Graphene-layered steps and their fields visualized by 4D electron microscopy

Sang Tae Park, Aycan Yurtsever, John Spencer Baskin, and Ahmed H. Zewail[1]

Physical Biology Center for Ultrafast Science and Technology, Arthur Amos Noyes Laboratory of Chemical Physics, California Institute of Technology, Pasadena, CA 91125

Contributed by Ahmed H. Zewail, April 9, 2013 (sent for review March 14, 2013)

Enhanced image contrast has been seen at graphene-layered steps a few nanometers in height by means of photon-induced near-field electron microscopy (PINEM) using synchronous femtosecond pulses of light and electrons. The observed steps are formed by the edges of graphene strips lying on the surface of a graphene substrate, where the strips are hundreds of nanometers in width and many micrometers in length. PINEM measurements reflect the interaction of imaging electrons and induced (near) electric fields at the steps, and this leads to a much higher contrast than that achieved in bright-field transmission electron microscopy imaging of the same strips. Theory and numerical simulations support the experimental PINEM findings and elucidate the nature of the electric field at the steps formed by the graphene layers. These results extend the range of applications of the experimental PINEM methodology, which has previously been demonstrated for spherical, cylindrical, and triangular nanostructures, to shapes of high aspect ratio (rectangular strips), as well as into the regime of atomic layer thicknesses.

atomic-scale steps | dark field imaging | photon-electron interaction | light scattering | discrete dipole approximation

The emerging field of photon-induced near-field electron microscopy (PINEM) relies on the interaction between the imaging electrons of an ultrafast electron microscope and the near-field components of scattered light pulses to reveal properties of nanoobjects and the induced optical fields surrounding them (1, 2). The experimental technique has been applied to a wide range of objects with differing material properties and different geometries, such as spheres, cylinders, triangular blocks, nanoparticles with irregular shapes, and for dimers of nanoparticles. The applications range from the visualization of the distribution of induced electric fields at the microscopic level to the enhancement of image contrast for biological structures (1–8).

Despite this progress, we did not expect to find that PINEM can be observed in a strip of carbon-based structures of only several atomic layers in thickness, a common materials structure studied by different variants of electron microscopy (9). Here, we report experimental and theoretical studies of graphene layered-step structures formed by the edges of strips of graphene multilayers lying on a continuous substrate of the same material, which give rise to an observed, strong PINEM intensity that is very strong when compared either with bright-field images in terms of relative contrast or with the PINEM intensity that could be obtained for a spherical or cylindrical geometry of the same thickness. This signal strength opens the door to the imaging of low–atomic-number, nanoscale materials using the enhanced contrast of PINEM. These low–atomic-number materials, such as carbon-based strips or cells, are weak elastic scatterers, making it a real challenge to obtain high contrast in, e.g., bright-field transmission electron microcopy (TEM). Dark-field imaging may be used to increase the image contrast, but the signal can be extremely low due to the low electron scattering probability. However, PINEM, which is based on an energy gain phenomenon, offers enhanced contrast due to its ability to selectively image discontinuities in the optical dielectric function.

The experimental techniques we use are those of PINEM imaging and its convergent-beam variant, ultrafast spectrum imaging (USI), as detailed in our previous publications (1, 3). These techniques are based on an inelastic interaction process between the probing ultrafast electron packets and the near fields induced by ultrafast laser pulses, in which electrons gain or lose energy in multiples of the photon energy. For the feasibility of these experiments, it is essential to have electrons, photons, and nanostructure all overlapping in space and time. The strongest imaging signal is achieved when the imaging electrons capture the ultrafast (femtosecond) near fields at their maxima. We note that the use of continuous-wave lasers for excitation would not provide the high interaction probability required to achieve the strong PINEM and USI imaging reported here.

PINEM and USI are complementary techniques, as they focus on spatial and energy distributions, respectively. Whereas PINEM is ideal for visualizing the real space distribution, it cannot be used to deduce the absolute cross-sections of the scattering process and, hence, the amplitude of the near fields. This limitation is inherent to parallel beam electron probing, such as PINEM, as the number of incident electrons at a given pixel is unknown. To overcome this restriction, the electron pulses can be focused to a nanoscale spot and scanned across the area of interest while at each position an energy gain spectrum is acquired. Because all of the scattered and unscattered electrons are contributing to the spectrum, the strength of the scattering cross-sections can be deduced from the relative experimental amplitudes of the energy-gain and zero-energy–loss peaks, with consideration of the temporal characteristics of the electron and light pulses.

The connection between the experimental observations reported here and the structural and material properties of the specimen is elucidated by first extending the theory of PINEM for symmetric structures (cylinders) to objects that are longitudinally very thin but laterally wide and infinitely long. A quantitative comparison with the measurements is then made by means of discrete dipole approximation (DDA) for a model graphene multilayer strip/graphene multilayer substrate system. For brevity, we will henceforth use graphene alone in referring to the samples studied here.

Results and Discussion

PINEM Measurements. Here, electron pulses were accelerated to 200 keV in an electron microscope equipped with electron energy loss spectrometry (EELS). The femtosecond light and electron pulses are overlapped at the specimen and can be scanned in time with an interferometry arrangement (10, 11). As described above, in a PINEM experiment, the electrons interact with the evanescent electric field resulting from the scattering of the incident light by

Author contributions: A.Y. and A.H.Z. designed research; S.T.P., A.Y., and J.S.B. performed research; S.T.P., A.Y., and J.S.B. analyzed data; and S.T.P., A.Y., J.S.B., and A.H.Z. wrote the paper.

The authors declare no conflict of interest.

Freely available online through the PNAS open access option.

[1]To whom correspondence should be addressed. E-mail: zewail@caltech.edu.

This article contains supporting information online at www.pnas.org/lookup/suppl/doi:10.1073/pnas.1306661110/-/DCSupplemental.

the specimen, gaining or losing energy in multiples of the photon energy, here 2.4 eV. With electron energy dispersion, the gain region can be resolved, thus providing the means for PINEM interactions to be detected and quantified (1, 2).

A schematic of the experimental geometry for the present study is shown in Fig. 1, where a graphene strip of width w and thickness (or height) h_1 is lying across a graphene sheet substrate of thickness h_2. The length of the strip, in the y direction, was much greater than its width, in the x direction. Values of h_1 and h_2 were each just a few nanometers, as determined by the characteristics of the inelastic plasmon loss signal in the static EELS (12, 13) (*SI Appendix, Part 1*). The lateral extent of the substrate, in the x–y plane, spanned the 6 μm × 6 μm openings in the supporting copper grid. The directions of propagation of the 519-nm laser and the electron beam were approximately parallel to each other (4° interbeam angle) and normal to the substrate's surface, i.e., along the z axis. The light wavelength and w were of similar magnitude and much greater than h_1 and h_2. The laser intensity was uniform over an area much wider than the opening in the supporting grid, and the area probed by the electron beam was varied, from 50 nm to 10 μm, for the different modes of data collection (USI and PINEM).

In Fig. 2, data are presented from one of the specimens studied. In the upper panels, two images of the same area are compared. On the left is a PINEM image, recorded using energy filtering to select a range encompassing the first four PINEM gain peaks; a TEM bright-field image is displayed on the right, with its contrast stretched by a factor of 2, for comparison. A graphite strip, a few nanometers in height and 590 nm in width, runs down the right side of the substrate, close to the copper grid bar. The PINEM image is essentially dark field, background free, with bright contrast clearly highlighting only certain features of the specimen, corresponding specifically to discontinuities in the dielectric function, which occur at structure edges. The PINEM intensity near such an edge depends on, among other things, the orientation of the linear polarization of the incident light relative to that edge (1, 2). It is high when the direction of the polarization, indicated in the figure by an arrow, is orthogonal to the edge, as is fairly close to the case here for both the strip edges and the edge of the grid bar.

In the lower panels of Fig. 2 are cross-sectional intensity profiles extracted from the same region in the two images given above, and indicated by the boxed areas in the images. Although the graphite strip is readily visible in the TEM image, it is seen in the corresponding profile that its relative image contrast differs from the substrate by only ∼5%. However, the PINEM intensity at the strip edges is a factor of 20–30 times as high as the residual background intensity from the flat substrate surface. The PINEM signal arises through the scattering fields generated by the discontinuity in the optical density at the graphene step, and its spread is tens of nanometers, whereas the bright-field image of the step is less than ∼10 nm wide. With high signal-to-noise ratio, it is possible to reconstruct the image with better spatial resolution, as done, e.g., in optical superresolution microscopy (14).

In addition to the strip, several other features are clearly revealed in the PINEM image that are far from evident in the TEM image. For example, the left end of each profile in Fig. 2 extends across a region that is very easily identified in the PINEM image as a discontinuity in the substrate uniformity by the two strong edge signals, with signal over background ratios greater than 8. This area (indicated by a gap in the profile box) in the bright-field image shows up with a barely discernible (∼1%) increase in contrast brightness above the background. From the increase in brightness, it must be concluded that some layers of the graphite substrate have been stripped away, leaving a pit. The contrast enhancement through the use of PINEM is more than a factor of 800 in this example.

To more accurately quantify the PINEM signal for a step-like feature, a USI study was carried out at three points near one edge of a different graphite strip (w, ∼1,000 nm). The results are given in Fig. 3. The thickness values of h_1 and h_2 in this case are 3.69–5.03 and 1.34–1.68 nm, respectively (for details, see *SI Appendix, Part 1*). A PINEM image of the area, the direction of light polarization, and the points at which the three energy-resolved spectra in the main panel were recorded are shown in *Insets*. Again, the polarization was nearly perpendicular (78°) to the strip

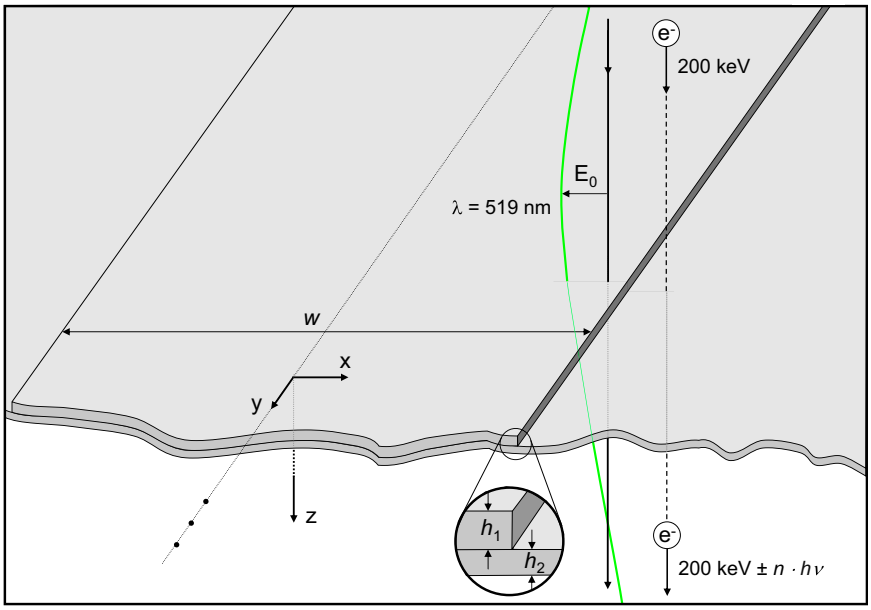

Fig. 1. Schematic of the experimental geometry. The graphite specimen consisted of a strip of width w and thickness h_1 lying across a larger sheet of thickness h_2, with values of h_1 and h_2 each a few nanometers. A 519-nm femtosecond laser pulse and 200-keV femtosecond electron pulse propagating along the normal to the specimen plane were coincident in space and time at the strip edge. The laser intensity was uniform over the entire specimen area, and the coverage of the electron beam varied with the experiment. See text for details.

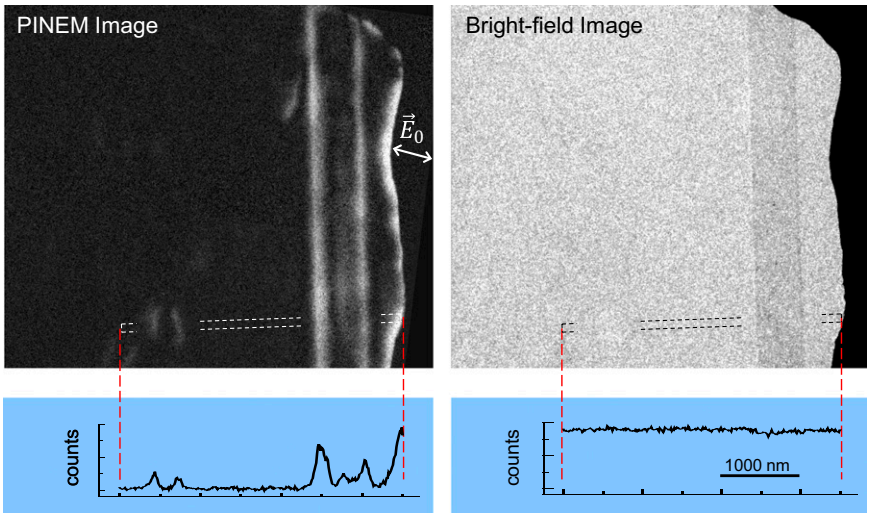

Fig. 2. Comparison of PINEM data and TEM bright-field data for the same area. (*Upper*) Images. The graphite specimen is bounded on the right by a copper grid bar. The dotted line boxes indicate the image area from which the profiles below were extracted. (*Lower*) Average image intensity profiles of the boxed area in the images. Intensities were averaged over the 10-pixel width of the boxes. The scale bar at *Lower Right* applies to the entire figure.

axis, resulting in a strong PINEM effect localized to the vicinity of the strip edges. The three spectra give the complete electron energy distributions at points on one strip boundary, and 50 and 100 nm away from it. Note that the amplitude of the gain and loss peaks in each spectrum correlates with the PINEM intensity at the corresponding image location. A cross-sectional profile of the image intensity along the horizontal dimension of the lower, expanded *Inset* of Fig. 3*A* is plotted in Fig. 3*B*, and the region associated with each spectrum measurement is indicated again, now by color-coded arrows. The theoretical solid lines fit all of the datasets in Fig. 3 *A* and *B*; the calculation details are discussed below.

The observations reported in Figs. 2 and 3 have temporal, spatial, and polarization dependencies that are in qualitative agreement with those reported in our previous experimental and theoretical studies of PINEM (1–8). However, the geometry of the structure studied here with its unique graphene thickness regime has not been examined in any of our previous work. Here, the minimum dimension (height) of the graphene strips is less than 5 nm, and smaller for the pit in Fig. 2, with transverse dimensions greater by two orders of magnitude or more. For such structures, with three vastly different dimensions, the theoretical results for spheres and cylinders, with thickness in the range of tens of nanometers, cannot be expected to provide any reliable and quantitative PINEM intensity calculations. It therefore becomes necessary to examine the PINEM dependence on the separate values of height and width, i.e., on the aspect ratio of the structure's cross-section, to achieve a complete understanding of the observations made.

Theory and Simulations. To elucidate the scattering properties of the nanoscale strip and to connect the observations with the dielectric properties of the structure, we have made the following theoretical development (for details, see *SI Appendix*, *Part 2*). In our model, the dielectric object (a strip with finite and independent width and height, and infinite length) is divided into a sum of infinitesimally small square beams, which are then approximated as infinite circular cylinders of an equal cross-sectional area. The induced polarizations of individual cylinders are determined by the incident light and scattering from the other cylindrical elements. The total scattering field is then obtained by summing contributions from all of the elements. The field integral, which represents the work performed by the scattering field on a passing electron (15), is evaluated by integrating the z component of the electric field, multiplied by a complex exponential factor of $e^{-i\Delta k_e z}$, where $\Delta k_e = \omega_p / v_e$ for light with angular frequency ω_p and an electron with velocity v_e. This term results from momentum conservation along the z axis, as detailed in ref. 2. The observed PINEM intensity varies approximately as the square of this field integral in the weak interaction limit (2). The electric polarization inside the strip is assumed to be uniform and is given by that of an elliptical cylinder of dimensions w and h:

$$P_x \approx \varepsilon_0 \frac{w+h}{w+h\varepsilon}(\varepsilon - 1), \qquad [1]$$

where ε is the dielectric constant of the material and ε_0 is the vacuum permittivity. Such an ellipsoid exhibits a polarization enhancement, of up to the ε value, when the aspect ratio, w/h, is large and incident light polarization is parallel to the width direction. Within this approximation, we only consider the near-field components of individual contributions. In this regime, we obtain an analytical expression for the electric field, and hence for the field integral, which is given by the following:

$$F \approx -\frac{i}{2} E_x^0 \left(\frac{w+h}{w+h\varepsilon}\right)(\varepsilon - 1)h\left\{e^{-\Delta k_e |x - w/2|} - e^{-\Delta k_e |x + w/2|}\right\}. \qquad [2]$$

Upon expansion of the terms in curly bracket (for $w \ll \Delta k_e^{-1}$), we obtain the following:

$$F \to -\frac{i}{2} E_x^0 \left(\frac{w+h}{w+h\varepsilon}\right)(\varepsilon - 1)(w \cdot h)\Delta k_e e^{-\Delta k_e x}, \qquad [3]$$

when x is larger than one-half the strip width ($w/2$). The elliptical approximation we used predicts that, for a narrow strip in the Rayleigh limit ($w \ll \lambda/2\pi$), the maximum magnitude of the field integral for a fixed aspect ratio is linearly proportional to the cross-sectional area ($w \cdot h$), but for a wide strip, the width dependence saturates around $\lambda/2\pi \cdot v_e/c$, which is 57 nm for our excitation wavelength. However, Eq. **2** only considers the near-field components, whereas the numerical field integral plateaus more slowly ($w = \sim 100$ nm) due to the far-field components (for details, see *SI Appendix*, *Part 2*).

From the above results, we can make an estimate of the comparative PINEM signal amplitudes for a 4-nm–diameter cylinder and a strip of 4 nm in height, both of graphite ($|\varepsilon|$ of ~10). The

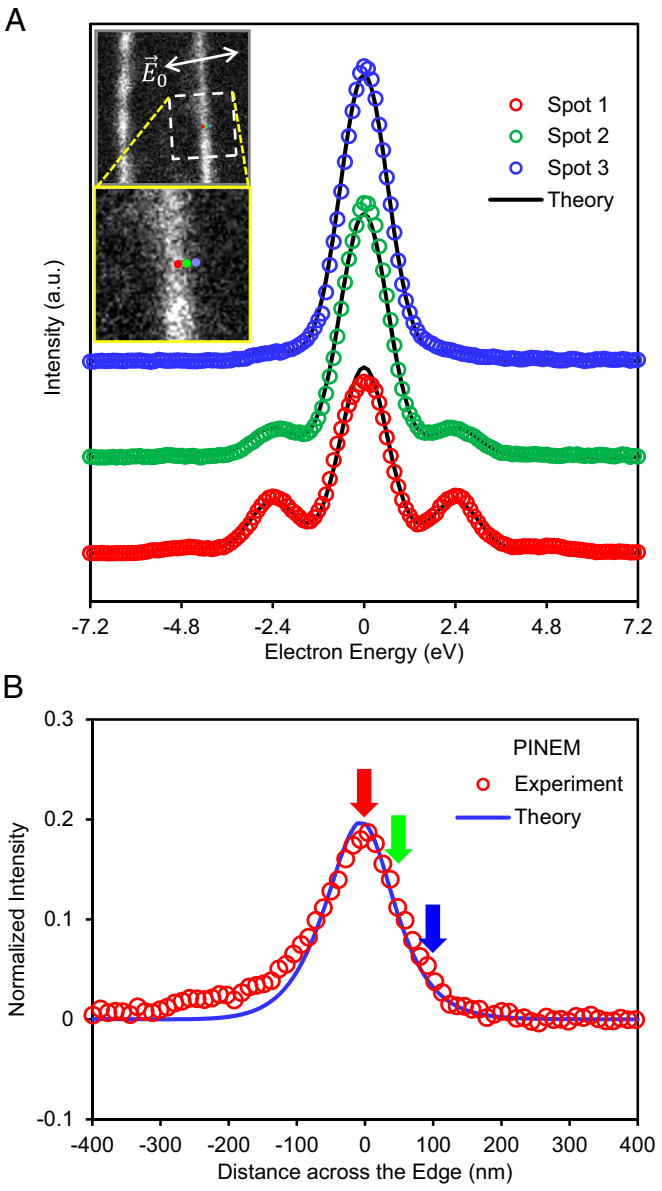

Fig. 3. Spatial and energy distributions of PINEM intensity at a graphene-layered step. (*A*) Three USI spectra give the complete electron energy distributions over 50-nm–diameter spots centered at one edge of a strip (spot 1), and 50 nm (spot 2) and 100 nm (spot 3) away from it, respectively. The laser and electron pulses were coincident in time at the specimen. (*Insets*) PINEM image of the area, the direction of light polarization, and the locations at which the three spectra in the main panel were recorded. *Lower Inset* is an enlargement of the area of the dotted line box in *Upper Inset*, and it is the image area from which the profile in *B* was extracted. (*B*) A profile of *y*-averaged image intensity along the width (*x* axis) of *Lower Inset* in *A* above. The centers of the regions corresponding to the USI spectra in *A* are indicated by arrows in the colors of the spectrum plots. The solid-line fits of all of the data sets are discussed in the text.

polarization enhancement factor in the field integral is ~5 and the cross-section enhancement is ~25 [from the ratio between the strip width dependence limit (~100 nm) and the cylinder diameter]. The total enhancement of ~125 for the integral results in a 15,000-fold difference in the expected PINEM signal at the edge of the strip vs. that at the edge of a cylinder of the same height.

Even though the elliptical approximation of a strip allows us to understand and calculate the strength of PINEM, a strip without a substrate does not accurately represent our experimental conditions. For a quantitative comparison, we need to consider the effect of the infinite substrate of a similar thickness (Fig. 1). Due to the high polarizability (susceptibility) of graphite, there is a strong interaction between the strip and the substrate, and, hence, the elliptical approximation described above is only partially valid. However, with the aid of numerical simulations, we can examine the validity of the approximation. In such a simulation, the polarization inside materials of an arbitrary shape is obtained by solving the matrix representing the scattering interaction with an incident wave using the DDA (16).

To simulate the light scattering of a graphene strip on an infinite substrate, we take the geometry as a 1-μm–wide band on a 5-μm–wide substrate. The heights of strip and substrate are set to be 4.03 and 1.34 nm, respectively (using multiples of the graphite unit cell height, 0.671 nm), values that are within the uncertainty ranges for the experimentally determined thicknesses of the specimen (Fig. 3). A grid size of 1.34 nm was used for practical computation times. Convergence of the field integral was checked with respect to the grid size, and the use of finer grid size only affects the result by 5%. The results of the simulation are plotted against the experimental observations in Fig. 3. To achieve good agreement in signal amplitude between the experiment and simulation, we scaled the laser intensity used in the simulation by a factor of 1.64 from that measured during the experiment. The shapes of the calculated curves were not sensitive to the assumed excitation fluence.

The above-mentioned calculations were made for a uniform planar specimen of infinite length in the *y* direction, resulting in a signal with no *y* dependence, but the experimental PINEM contrast along all strip edges is seen to vary by at least a factor of 2 (Figs. 2 and 3*A*, *Inset*). The variations observed in the experimental intensity are believed to be due to nonuniformity of the strip and substrate and to effects associated with the finite length of the strip, and these factors are currently the subject of experimental and theoretical investigations in our laboratory. Nevertheless, it is clear that the theory reproduces reasonably well the characteristics of the experimental PINEM signals for the graphene specimen.

The physical picture provided by the DDA simulations used for matching the experimental observations is presented in Fig. 4; for comparison, calculations for other geometries are also included. The three shapes considered are as follows: a 4-nm–diameter cylinder, a thin isolated strip 4 nm in height, and our model system, the same strip on a 1.3-nm substrate. The top panels of the figure show vector plots of the scattered electric field amplitudes in the *x*–*z* plane. Dashed-line cross-sections of the structures are shown in the panels. The real and imaginary components of the field arise as a consequence of graphite's complex index of refraction. Note that the arrows in the vector plot of the cylinder are expanded relative to those of the strips by a factor of 20. The green color density represents the total field amplitude on a common scale for the three structures, for the purpose of direct comparison. The middle panels of the figure show in detail the field dependence along the *z* direction in the *y*–*z* planes that are tangent to the right edge of each structure.

Fig. 4 *A* and *D* depict the scattering by a cylinder, where the spatial profile of the near-field component is in the form of a static line-dipole, which is different in the angular distribution from that of far-field Rayleigh scattering. Fig. 4 *B* and *E* show scattering from an isolated strip, where an almost uniform polarization gives rise to a charge buildup at the edge and, hence, to a near-field profile like that of a line-monopole charge because the opposite edge is far away on the scale of the figure. In Fig. 4 *C* and *F*, the substrate changes the induced polarization of the isolated strip such that the scattered field is weaker than that of the strip alone. For a line-dipole with a small separation of the charges (cylinder; Fig. 4*A*), the electric field contributions of the nearby opposite charges, substantially cancel each other, resulting in a weak electric field of scattered light that decays with r^{-2}.

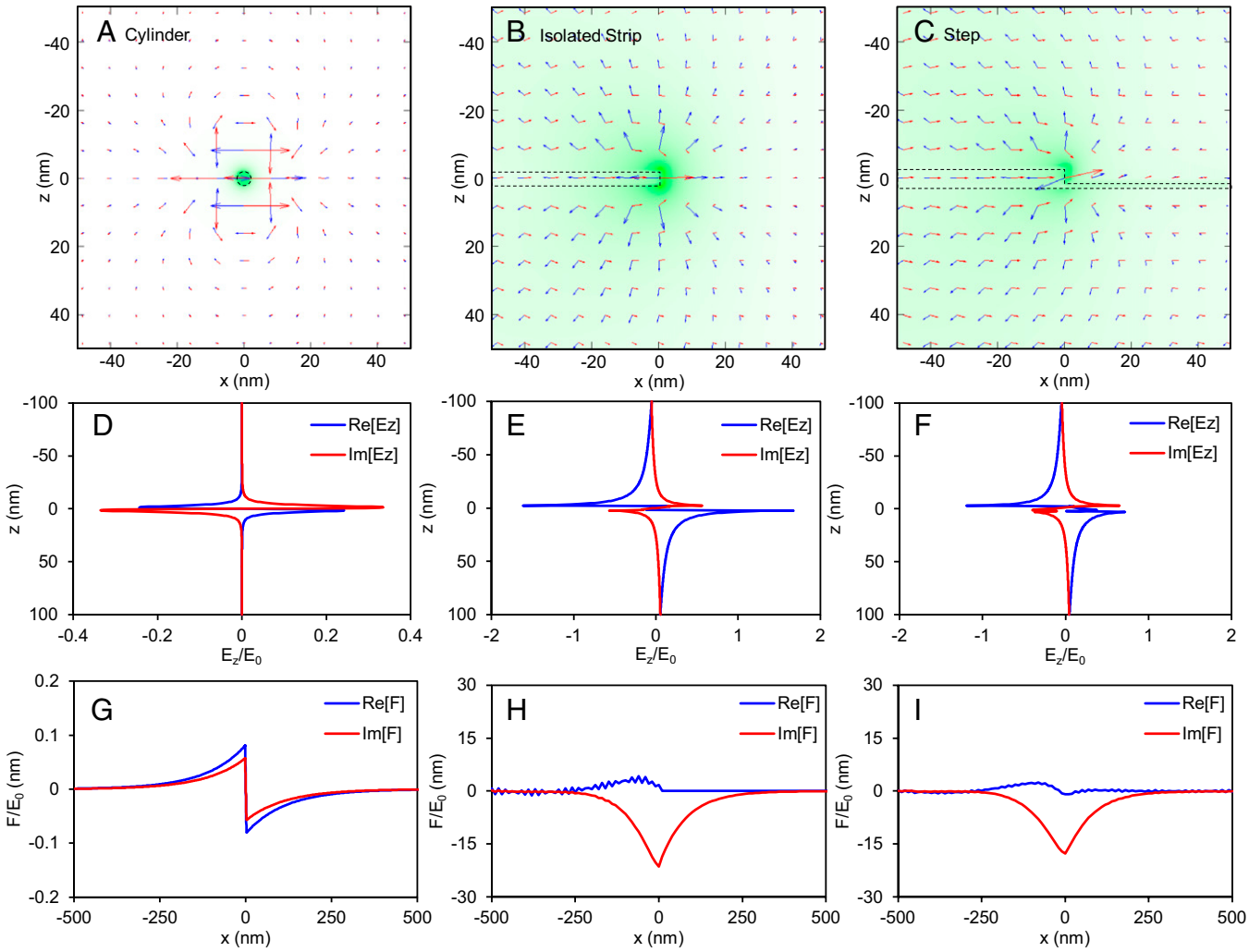

Fig. 4. Spatial distributions of fields and field integrals from DDA simulations of the response to scattered light of three graphite nanostructures. Blue and red are used to indicate the real and imaginary components of the respective quantities. (*A–C*) Vector plots of the electric fields of scattered light of (*A*) a cylinder, (*B*) the edge of a thin strip, and (*C*) a layered step. The cross-sections of the structures are shown as dashed outlines. Green color density indicates the field magnitude. The arrows in *A* are expanded by a factor of 20 relative to those in *B* and *C*. See text for details. (*D–F*) Line plots of the *z* component of the electric fields of scattered light along the *z* axis at the right edge of each of the three structures of *A–C*. (*G–I*) Line plots of the PINEM field integrals as a function of *x* for the same three structures. The *x* axes are all expanded from those of plots in *A–C*.

In comparison, for an effective line-monopole (strip; Fig. 4*B*) due to the distance of the opposite charge, there is no cancellation and the field attenuates more slowly (r^{-1}).

The bottom row of Fig. 4 displays plots of the *x* dependence of the field integral for the three structures. As shown in our previous publications (2), for a small cylinder, the field integral exponentially decays from both edges with a decay length of ~80 nm, regardless of its radius (Fig. 4*G*). When the electron trajectory goes through the cylinder, the field integral rapidly decreases and vanishes at its center. Overall, the field integral is antisymmetric with respect to the center of the cylinder, along the *x* direction. In contrast, the field integral at each edge of a strip decays exponentially and symmetrically from the position of the edge (Fig. 2). This behavior, as described in Eq. **2**, is seen in Fig. 4*H*, where here the strip right edge is at $x = 0$ rather than $w/2$.

The field integral of the strip is antisymmetric with respect to the center of the strip (*SI Appendix*, Fig. S5). Even though the peak magnitude of the field around the monopole is only a few times larger than that of the cylinder (Fig. 4 *D* and *E*), the field integral is much larger than that of the cylinder, because the field is persistent over a larger range of *z* and the monopoles (strip edges) spaced beyond ~100 nm do not cancel each other's contributions as they do for a small cylinder. For a small cylinder, two line-monopoles are close together and their opposite-signed contributions to the field integral, which decay slowly, almost completely cancel each other, resulting in a greatly reduced amplitude (by two orders of magnitude). This very strong cancellation also causes a steep linear behavior around the center inside the cylinder. In Fig. 4*I*, the spatial profile of the field integral of the strip/substrate structure is similar to that of the strip, but its magnitude is smaller, as discussed above.

As stated above, the much larger magnitude of the field integral for the strip relative to that for the cylinder, is attributed not to the moderate increase in peak magnitude of the field but to the much slower decay of the field in the *z* direction. Furthermore, it is imperative to note that, because of the particular form of *z* integration, the field integral is relatively insensitive to the electric field nearest the particle (z, ~0), where the scattering fields are strongest. In other words, the PINEM is most sensitive to the distant field of the near field component of the scattered light. The distant field is more dependent on *z* than on *x*, and that is why the field integral for an infinitely long object decays more

slowly (~100 nm), even though the electric field itself decays faster, on the order of the particle thickness (<10 nm here).

Conclusion and Outlook

We have shown, both experimentally and theoretically, that high-contrast imaging of nanoscale graphene-layered steps is possible by means of the PINEM technique, which enables visualization of the induced electric, near fields through their interaction with ultrafast imaging electrons. Although these steps are only several atomic layers, it was shown that the high aspect ratio, and large total cross-section, greatly enhances the field integral and thus the PINEM image contrast. This enhancement is particularly significant, especially when imaging thin carbon-based materials. We expect this work to pave the way for high-contrast imaging of soft materials that are otherwise weak scatterers. Besides the enhancement in imaging, PINEM visualization of near fields of atomic-scale systems should prove useful in the studies of networks of nanoplasmonics and photonics, with possible applications ranging from molecular sensors (17) to high-efficiency solar cells (18), whose functions rely on their ability to focus electromagnetic energy into very small volumes (19–21). Last, atomic-scale steps are known for their unique involvement in catalysis, and mapping the fields at the steps is critical for understanding the structure and timescales involved. The combinations of real-space, energy-space, and reciprocal-space imaging in 4D ultrafast electron microscopy make it possible to explore other applications in various fields (9, 22).

Materials and Methods

Commercially available graphene specimens were purchased from Graphene Supermarket. The graphene-layered strips were observed to occur at random locations on the substrates. Thicknesses were determined by comparisons of the plasmon loss regions of static EEL spectra with similar spectra recorded for graphene specimens of known thickness (13). Examples of thickness determination are given in *SI Appendix, Part 1*.

The UEM-2 apparatus has been described in detail elsewhere (10, 11). We used light pulses of two different wavelengths: the 259-nm pulse that was sent to the cathode (to extract the probing photoelectrons) and the 519 nm, which was directed to the specimen, both produced by harmonic generation from the 1,038-nm output of a variable repetition rate fiber oscillator–amplifier femtosecond laser system. The direction of polarization of the excitation pulse was controlled by a half-wave plate at the entrance to the microscope. A variable optical delay line was used to establish a well-defined and adjustable temporal delay between the exciting photon pulses and the probing electron pulses at the specimen. The PINEM interaction between the electron and the photon is maximum when the ultrafast electrons and photons are overlapped in space and when the delay time between them is zero, i.e., $t_d = 0$. The PINEM effect becomes significantly weaker for delays of a few hundred femtoseconds, earlier or later than the optimal delay ($t_d = 0$) and disappears for $|t_d| > 1$ ps (1).

In the energy-resolved spectra, clear resolution of electrons that have undergone energy gain or loss upon traversing the specimen is only possible when the energy spread of the zero-loss peak (ZLP) is narrower than the amount of energy gained or lost, which in the PINEM experiments is the photon energy (here, 2.4 eV). To achieve this condition, it was necessary to avoid electron energy spread caused by space charge repulsion within the propagating electron packets. This, in turn, was achieved by reduction of the UV laser intensity on the cathode to restrict the electron count in each pulse, resulting in a ZLP with a typical full width at half-maxima (FWHM) of ~1.4 eV. The low electron counts, referred to as the single electron per pulse condition, also limited space charge-induced temporal electron spread, leading here to an electron pulse temporal width of ~500 fs at the specimen.

Under single-electron conditions, images and energy-resolved spectra with adequate electron counts were acquired stroboscopically by repeating the excitation-and-probing cycle under fixed conditions typically tens of millions of times. Up to 10 frames were acquired, corrected for drift, and summed to improve signal to noise. To ensure stability and allow for quantitative analysis, the laser characteristics at the specimen, including power, spot size, and location, were monitored continuously throughout all experiments. Laser repetition rates of 400 kHz and 1 MHz were used, with the power of the visible pulse on the specimen restricted to levels that produced no cumulative damage over the course of data acquisition. In all cases, the diameter of the laser focus on the specimen (FWHM of ~35 μm) was much larger than the area probed by the electrons, so the irradiation may be considered to be uniform, with typical pulse fluence of ~4.5 mJ/cm^2.

Two types of data were collected for this study, with t_d fixed at zero in both cases. PINEM images of areas several micrometers in extent were recorded using energy filtering to select an energy range of +2 to +12 eV above the center of the ZLP, encompassing the first four PINEM gain peaks. In these data, brightness in the images correlates to the local strength of the electron–photon interaction and, hence, to the presence of localized near fields. In the second type of data, ultrafast spectrum imaging with convergent beams was used, where energy-resolved spectra of the low gain and loss regions near the ZLP were recorded at specific locations of interest on the specimen by collimating the electron beam to a 50-nm–diameter spot.

ACKNOWLEDGMENTS. This work was supported by National Science Foundation Grant DMR-0964886 and Air Force Office of Scientific Research Grant FA9550-11-1-0055 for research conducted in The Gordon and Betty Moore Center for Physical Biology at the California Institute of Technology.

1. Barwick B, Flannigan DJ, Zewail AH (2009) Photon-induced near-field electron microscopy. *Nature* 462(7275):902–906.
2. Park ST, Lin MM, Zewail AH (2010) Photon-induced near-field electron microscopy (PINEM): Theoretical and experimental. *New J Phys* 12:123028.
3. Yurtsever A, van der Veen RM, Zewail AH (2012) Subparticle ultrafast spectrum imaging in 4D electron microscopy. *Science* 335(6064):59–64.
4. Yurtsever A, Zewail AH (2012) Direct visualization of near-fields in nanoplasmonics and nanophotonics. *Nano Lett* 12(6):3334–3338.
5. Yurtsever A, Baskin JS, Zewail AH (2012) Entangled nanoparticles: Discovery by visualization in 4D electron microscopy. *Nano Lett* 12(9):5027–5032.
6. Flannigan DJ, Barwick B, Zewail AH (2010) Biological imaging with 4D ultrafast electron microscopy. *Proc Natl Acad Sci USA* 107(22):9933–9937.
7. Park ST, Kwon OH, Zewail AH (2012) Chirped imaging pulses in four-dimensional electron microscopy: Femtosecond pulsed hole burning. *New J Phys* 14:053046.
8. Park ST, Zewail AH (2012) Enhancing image contrast and slicing electron pulses in 4D near field electron microscopy. *Chem Phys Lett* 521:1–6.
9. Thomas JM, Midgley PA (2011) The modern electron microscope: A cornucopia of chemico-physical insights. *Chem Phys* 385(1–3):1–10.
10. Park HS, Baskin JS, Kwon OH, Zewail AH (2007) Atomic-scale imaging in real and energy space developed in ultrafast electron microscopy. *Nano Lett* 7(9):2545–2551.
11. Barwick B, Park HS, Kwon OH, Baskin JS, Zewail AH (2008) 4D imaging of transient structures and morphologies in ultrafast electron microscopy. *Science* 322(5905):1227–1231.
12. Egerton RF (1996) *Electron Energy-Loss Spectroscopy in the Electron Microscope* (Plenum, New York), 2nd Ed.
13. Eberlein T, et al. (2008) Plasmon spectroscopy of free-standing graphene films. *Phys Rev B* 77(23):233406.
14. Lubeck E, Cai L (2012) Single-cell systems biology by super-resolution imaging and combinatorial labeling. *Nat Methods* 9(7):743–748.
15. Park ST, Zewail AH (2012) Relativistic effects in photon-induced near field electron microscopy. *J Phys Chem A* 116(46):11128–11133.
16. Draine BT (1988) The discrete-dipole approximation and its application to interstellar graphite grains. *Astrophys J* 333(2):848–872.
17. Liu N, Tang ML, Hentschel M, Giessen H, Alivisatos AP (2011) Nanoantenna-enhanced gas sensing in a single tailored nanofocus. *Nat Mater* 10(8):631–636.
18. Aubry A, et al. (2010) Plasmonic light-harvesting devices over the whole visible spectrum. *Nano Lett* 10(7):2574–2579.
19. Maier SA (2007) *Plasmonics: Fundamentals and Applications* (Springer, New York).
20. Prasad PN (2004) *Nanophotonics* (Wiley-Interscience, Hoboken, NJ).
21. Dionne JA, Atwater HA (2012) Plasmonics: Metal-worthy methods and materials in nanophotonics. *MRS Bull* 37(8):717–724.
22. Thomas JM (2009) The renaissance and promise of electron energy-loss spectroscopy. *Angew Chem Int Ed Engl* 48(47):8824–8826.